Optimally amplified large-scale streaks and drag reduction in turbulent pipe flow

Ashley P. Willis[*] and Yongyun Hwang[†]

Laboratoire d'Hydrodynamique (LadHyX), École Polytechnique, 91128 Palaiseau, France

Carlo Cossu[‡]

*Institut de Mécanique des Fluides de Toulouse (IMFT), 31400 Toulouse, France and Département de Mécanique,
École Polytechnique, 91128 Palaiseau, France*

The optimal amplifications of small coherent perturbations within turbulent pipe flow are computed for Reynolds numbers up to one million. Three standard frameworks are considered: the optimal growth of an initial condition, the response to harmonic forcing and the Karhunen-Loève (proper orthogonal decomposition) analysis of the response to stochastic forcing. Similar to analyses of the turbulent plane channel flow and boundary layer, it is found that streaks elongated in the streamwise direction can be greatly amplified from quasistreamwise vortices, despite linear stability of the mean flow profile. The most responsive perturbations are streamwise uniform and, for sufficiently large Reynolds number, the most responsive azimuthal mode is of wave number $m=1$. The response of this mode increases with the Reynolds number. A secondary peak, where m corresponds to azimuthal wavelengths $\lambda_\theta^+ \approx 70-90$ in wall units, also exists in the amplification of initial conditions and in premultiplied response curves for the forced problems. Direct numerical simulations at Re $=5300$ confirm that the forcing of $m=1,2$ and $m=4$ optimal structures results in the large response of coherent large-scale streaks. For moderate amplitudes of the forcing, low-speed streaks become narrower and more energetic, whereas high-speed streaks become more spread. It is further shown that drag reduction can be achieved by forcing steady large-scale structures, as anticipated from earlier investigations. Here the energy balance is calculated. At Re$=5300$ it is shown that, due to the small power required by the forcing of optimal structures, a net power saving of the order of 10% can be achieved following this approach, which could be relevant for practical applications.

I. INTRODUCTION

The nature of laminar-turbulent transition, and of the structure of turbulence in pipe flow, is a subject that has interested generations of fluid dynamicists since the pioneering work of Reynolds [1]. Laminar pipe flow (the Hagen-Poiseuille flow solution) is linearly stable, but subcritical transition to turbulence is observed at Reynolds numbers as low as ≈ 2000. A key mechanism in the transition process is played by the lift-up effect [2,3] consisting of the strong amplification of the energy of streamwise streaks that evolve from streamwise vortices. These streaks are narrow elongated regions where the streamwise velocity is larger or smaller that the average at the same distance from the wall. The large amplification of the streaks by the lift-up mechanism is related to the strong non-normality of the linearized Navier–Stokes operator [4–6]. Optimal perturbations, which maximize the energy amplifications, have been computed for most of the canonical laminar shear flows, where it is found that streamwise uniform structures are the most amplified. The maximum amplification of initial conditions, and responses to harmonic and stochastic forcing have been found to scale such as Re^2, Re^4, and Re^3, respectively [6–9]. For laminar pipe flow, the most amplified streamwise uniform

modes are those of azimuthal wave number $m=1$ [10–12], decreasing monotonically with increasing m, and the resulting streaks are significantly unstable when of sufficient amplitude [13].

Coherent streaky motions also exist in the turbulent pipe. The existence of streaks in the buffer layer with a mean spanwise spacing of ≈ 100 wall units has been well documented for the boundary layer [14–16] and for pipe flows [17,18]. Coherent streaky structures exist also at much larger scales, of the order of several pipe radii, R. Recently it has been realized that these structures can be very long (at least $\approx 8R$ to $16R$), and contribute to half of the total turbulent kinetic energy and Reynolds stress [19,20]. Contrary to other canonical turbulent flows, for the case of the turbulent pipe relatively little is known on the spanwise (azimuthal) structure of these coherent large-scale structures.

While early computations of optimal growths and responses to stochastic forcing [21–23] have considered the turbulent mean flow as a base flow, the molecular viscosity was included in the equations for the coherent perturbations. An externally imposed eddy turnover time had to be included in the optimization process. More recent analyses of the turbulent plane channel flow [24–26], boundary layer [27] and Couette flow [28] have included the effect of the eddy viscosity in the linearized equations, in the spirit of Ref. [29]. In this approach the eddy turnover time need not be enforced, but is an output of the optimization process. Following this approach, two preferred spanwise wavelengths are found for the amplification of streamwise uniform streaks, for sufficiently high Reynolds numbers. The first ($\lambda_z \approx 3h$ to $4h$ for

———————
*willis@ladhyx.polytechnique.fr
†yongyun@ladhyx.polytechnique.fr
‡carlo.cossu@imft.fr

plane channel flow) scales in outer units (i.e., with the channel half-width h), and the maximum amplifications increase with the Reynolds number. The second preferred spanwise length, which scales in inner (wall) units, is found at $\lambda^+ \approx 100$, in good accordance with the scales of the buffer layer cycles. Here milder energy amplification of initial conditions is found. These results strongly suggest that the mean lift-up effect is involved as an essential part of the mechanisms that permit the sustanance of turbulent coherent structures.

When streaks are of finite amplitude they may support the amplification of secondary perturbations [30,31] that lead to their breakdown, and to the refueling of streamwise vorticity necessary to sustain the streaks [32,33]. This self-sustained process is christened in the emergence of nonlinear saddle solutions [34,35] and unstable periodic orbits [36]. Many unstable nonlinear solutions have also been found for pipe flow [37,38], where a positive Lyapunov exponent is displayed in the turbulent regime [39]. These "exact" solutions [40], which are believed to provide a structure to the subcritical transition process [41], typically have few unstable eigenvalues and associated modes, while they are attracting in all other directions in phase space. It has therefore been conjectured that transitional flow spends significant periods of time in the neighborhood of a few of these nonlinear solutions, and that therefore the lowest order statistics could be retrieved by averaging over the exact solutions. This rational framework has been boosted by the experimental observation of the velocity field bearing resemblance to exact nonlinear traveling wave solutions [42]. Exciting phase space portraits of the transitional regime are becoming available for the plane Couette flow [43].

It is currently not clear how to extend the dynamical systems approach into the régime of developed turbulence. At large Reynolds numbers, exact solutions typically have high wave numbers, implying an unrealistic number of repetitions of the structure in space. Progress is being made with respect to this spatial dependence, with the discovery of localized counterparts to the infinitely extended solutions [44]. Other periodic solutions have been continued to high Reynolds numbers [45]. A different but serious problem is that, while capturing the typical features of turbulence near the wall, exact solutions do not exhibit the large dissipation of turbulence in the central region of the flow. It is this dissipation that leads to flattened mean profiles of the flow and strong deceleration of the core region for pipe flow. This slow core is clearly present in the observations of [42]. While dissipation occurs on small scales in the central region, however, coherent streaks certainly are present. A myriad of solutions exhibiting streaks is now available for pipe flow [46], but it is not yet clear how to determine which best characterize turbulence. Toward this end, in the present study the eddy viscosity is invoked to help reveal on which length scales the most important structures occur, those associated with energy production through amplification, and who's presence may otherwise be masked by the dissipative eddies.

In addition to its potential relevance for understanding the structure of turbulent flows, the analysis of optimal energy amplifications is also relevant for flow control. In the laminar boundary layer, for instance, the forcing of nearly optimal streaks has been used to stabilize the base flow to Tollmien-Schlichting waves [47–49] and delay transition to turbulence [50]. That large-scale coherent streaks can be effectively amplified in the turbulent boundary layer [51,52] has opened the way for their use in separation control in industrial applications [53]. Furthermore, a few studies [54,55] have shown that by forcing large-scale streamwise vortices, viscous drag can be reduced in the plane channel flow. However, in these studies the cost of the control action has not been evaluated, and it is therefore unclear if a net power saving can be achieved. In this study, the advantage of forcing optimal structures is that the energy required for the forcing is minimized, reducing the cost of the control.

The scope of the present investigations is therefore to answer the following questions: what are the optimal energy amplifications and responses to forcing sustained by the mean turbulent flow in a pipe? Structures of which wavelengths are most amplified? And, how do these amplifications and their structure change with Reynolds number? Despite its ubiquity in practical applications, these results are not yet available for turbulent pipe flow. A linear model is presented in Sec. II. Linear results (Sec. III), based on the eddy-viscosity model, here and for the planar geometries, are yet to be compared with simulations of "real" turbulence, i.e., in full resolved simulation (Sec. IV). In other words, do the optimal streaks predicted by the linear eddy-viscosity model compare well to artificially forced streaks computed in direct numerical simulation? As simulations in the presence of turbulence are inherently nonlinear, what is the effect of finite amplitude forcing on these coherent streaks? Finally, we are interested in the influence of artificially forced finite amplitude streaks on the drag. Can the mean drag be reduced in the presence of large amplitude streaks? Is a net power saving, including the cost of the control, achievable, and if so, what is the best performance?

II. BACKGROUND

A. Turbulent base flow and eddy viscosity

Consider the incompressible flow of a viscous fluid of kinematic viscosity ν in a circular pipe of radius R. The bulk velocity U_b (mean streamwise speed) is assumed constant. Lengths are nondimensionalized by R and velocities by $U_{cl}^{lam} = 2U_b$, the center-line speed for laminar flow of the same bulk velocity [12,38,56,57]. The usual Reynolds number based on the mass flux is defined as $\mathrm{Re} = 2U_b R/\nu$. At sufficiently large Reynolds numbers the flow is turbulent and the turbulent mean flow profile preserves invariance in the spanwise direction θ, the streamwise direction x, and in time t. The mean flow velocity is written $\boldsymbol{U} = U(y)\boldsymbol{e}_x$, where $y = 1 - r$ is the dimensionless distance from the boundary wall and r is the radial coordinate. In complement to this "outer" scaling, convenient for measuring large-scale properties, to describe near-wall structure it is commonplace to also define units via the friction velocity $u_\tau^2 = \nu \partial_y U|_{y=0}$, based on the shear near the wall. The wall units of length and time are then ν/u_τ and ν/u_τ^2, respectively. Variables nondimensionalized on this "inner" scaling bare the superscript + in the following, and the wall-Reynolds number is defined $\mathrm{Re}_\tau = u_\tau R/\nu$.

If, as a first approximation, the Boussinesq eddy viscosity is used to model the turbulent Reynolds-stresses, then the streamwise component of the Reynolds-averaged momentum conservation reads

$$\frac{1}{\text{Re}}\left(\frac{1}{r}+\partial_r\right)(\nu_T\partial_r U)=\partial_x P, \tag{1}$$

where the total effective viscosity is $\nu_T(y)=1+E(y)$ and $E(y)$ is the eddy-viscosity, normalized such that at the wall $\nu_T(0)=1$, i.e., the kinematic value is attained. We denote by $B=-\partial_x P$, the averaged streamwise pressure gradient necessary to maintain the prescribed mass flux.

For $E(y)$ we use the convenient expression originally suggested for pipe flow by Cess [58], later used for channel flows by Reynolds and Tiederman [59], then by many others [21,24,25]:

$$E(y)=\frac{1}{2}\left\{1+\frac{\kappa^2\hat{R}^2\hat{B}}{9}[2y-y^2]^2(3-4y+2y^2)^2\right.$$
$$\left.\times\left[1-\exp\left(\frac{-y\hat{R}\sqrt{\hat{B}}}{A^+}\right)\right]^2\right\}^{1/2}-\frac{1}{2}. \tag{2}$$

The mean streamwise velocity $U(y)$ in equilibrium with this radially dependent eddy viscosity [Eq. (2)] is easily inverted from the mean averaged momentum Eq. (1), and matches very well experimental observations. Here, $\hat{R}=\text{Re}/2$, $\hat{B}=2B$. The fitting parameters $A^+=27$ and $\kappa=0.42$ have been updated to improve the match with recent observations in [60].

B. Equations for the small coherent perturbations to the turbulent base flow

We now take the state $\mathbf{\Phi}=(U,P)$, solution of Eq. (1), as a (steady) base flow and consider small coherent (correlated when ensemble-averaged) perturbations, $\boldsymbol{\varphi}=(\boldsymbol{u},p)$, to $\mathbf{\Phi}$ in the presence of a coherent (correlated) force $\boldsymbol{f}$ and/or coherent initial conditions $\boldsymbol{u}_0$. Note that $\mathbf{\Phi}$ is understood to be the turbulent mean state for $\boldsymbol{f}=\boldsymbol{0}$ and $\boldsymbol{u}_0=\boldsymbol{0}$.

The equations governing the coherent perturbations require modeling of the Reynolds stresses to be closed. Reynolds and Hussain [29] discussed the eddy viscosity as a simple closure model, finding that it compared well for small-amplitude perturbations. Linearizing the closed equations, following [24–29], the equation governing small-amplitude coherent perturbations is

$$\partial_t\boldsymbol{u}+u_r\partial_r U\boldsymbol{e}_x+U\partial_x\boldsymbol{u}=-\boldsymbol{\nabla}p+\frac{1}{\text{Re}}\boldsymbol{\nabla}\cdot[\nu_T(y)(\nabla\boldsymbol{u}+\nabla\boldsymbol{u}^T)]$$
$$+\boldsymbol{f}. \tag{3}$$

These perturbations also satisfy continuity, $\boldsymbol{\nabla}\cdot\boldsymbol{u}=0$. The explicit components for the viscous term are given in Appendix A.

Exploiting the rotational and the streamwise translational invariance of the system, one may expand the perturbations in Fourier modes $\boldsymbol{\varphi}(r,\theta,x;t)=\Sigma_{\alpha m}\hat{\boldsymbol{\phi}}_{\alpha m}(r;t)e^{i(\alpha x+m\theta)}$, where α and m are the streamwise and azimuthal wave number respectively. Substitution into Eq. (3) gives

$$\partial_t\hat{\boldsymbol{\phi}}_{\alpha m}(r;t)=\boldsymbol{L}_{\alpha m}(\mathbf{\Phi})\hat{\boldsymbol{\phi}}_{\alpha m}+\hat{\boldsymbol{f}}_{\alpha m}(r;t), \tag{4}$$

where $\boldsymbol{L}_{\alpha m}$ is the linear operator acting on the Fourier mode $\hat{\boldsymbol{\phi}}_{\alpha m}(r)$. The problem may be considered for each mode independently, and the subscript α,m is dropped in the following. The spanwise and streamwise wavelengths for each perturbation are given by $\lambda_\theta=2\pi/m$ and $\lambda_x=2\pi/\alpha$ respectively in units of R.

C. Optimal growth and response to forcing

Three properties of the linearized system are now examined. They are the optimised growth of initial conditions, the optimised response to harmonic forcing, and the response to stochastic forcing. Standard definitions (see, e.g., [6,61]) are briefly restated below for the present context.

Optimal growth in time over all possible nonzero initial conditions $\hat{\boldsymbol{u}}_0$, for a particular α,m mode, is given by the function

$$G(\alpha,m;t)\equiv\max_{\hat{\boldsymbol{u}}_0\neq\boldsymbol{0}}\frac{\|\hat{\boldsymbol{u}}(t)\|^2}{\|\hat{\boldsymbol{u}}_0\|^2}, \tag{5}$$

and the maximum achieved over all times is $G_{\max}(\alpha,m)\equiv\max_t G(\alpha,m;t)$. Here $\hat{\boldsymbol{f}}=\boldsymbol{0}$, and the energy norm used is $\|\hat{\boldsymbol{u}}\|^2\equiv(1/V)\int_V\boldsymbol{u}\cdot\boldsymbol{u}\,dV$.

For harmonic forcing, $\hat{\boldsymbol{f}}=\tilde{\boldsymbol{f}}e^{i\Omega_f t}$, and accompanying response, $\hat{\boldsymbol{u}}=\tilde{\boldsymbol{u}}e^{i\Omega_f t}$, the optimal response is given by

$$R(\alpha,m;\Omega_f)\equiv\max_{\tilde{\boldsymbol{f}}\neq\boldsymbol{0}}\frac{\|\tilde{\boldsymbol{u}}\|^2}{\|\tilde{\boldsymbol{f}}\|^2}. \tag{6}$$

The maximum over all frequencies Ω_f is $R_{\max}(\alpha,m)=\max_{\Omega_f}R(\alpha,m;\Omega_f)$.

Finally, the response to a stochastic force is usually considered in the discretized form (here radially). Let $\hat{\boldsymbol{f}}(t)$ be the discretized stochastic force vector, and $\langle\cdot\rangle$ denote ensemble averaging. Following analyses [9,22,61–64], the forcing is assumed to have Gaussian probability density with zero average (i.e., $\langle\hat{\boldsymbol{f}}\rangle=\boldsymbol{0}$), isotropic (equal variance on all the three components) and delta-correlated in space and time, $\langle\hat{\boldsymbol{f}}(t)\hat{\boldsymbol{f}}^H(t')\rangle=\mathbf{I}\delta(t-t')$, where the superscript H denotes the Hermitian transpose. The amplification of the stochastic forcing is then measured by the variance of the response:

$$V(\alpha,m)\equiv tr\{\mathbf{C}_\infty\}, \tag{7}$$

where $\mathbf{C}_\infty=\langle\hat{\boldsymbol{u}}\hat{\boldsymbol{u}}^H\rangle$ is the covariance matrix for the response in the limit $t\to\infty$. This covariance matrix is computed by solving an algebraic Lyapunov equation (see Appendix B). The eigenfunction decomposition of the Hermitian matrix $\mathbf{C}_\infty$ is known as the Karhunen-Loève (KL) or proper orthogonal decomposition (POD). The ratio of its real and positive eigenvalues, σ_n, to the variance $V=\Sigma_n\sigma_n$ represent the relative contribution to the variance from each orthogonal mode. The eigenfunction corresponding to the leading eigenvalue thus contributes most to the variance V. For details see [9,22,62–65].

D. Numerical methodology

The linear operator appearing in Eq. (3) must be discretized in order to compute the optimal growths and the responses described above. Some attention must be paid to difficulties introduced by the cylindrical geometry, and full details of the methods are given in Appendix B. Here we note the general approach and convergence of the results.

A Chebyshev-collocation method on up to $N=250$ radial points was used to calculate up to $2N-3$ eigenvectors and eigenvalues for the linear system [Eq. (3)]. The optimal growth code, which requires only these eigenvectors, eigenvalues and weights for calculating norms, is a well validated code used for several previous studies [25,27,28,66]. Results for the optimal growth and the response to steady forcing were also verified by direct time stepping. At the largest $Re=10^6$ the power spectral drop-off for the optimal modes was of eight orders of magnitude.

Responses from the linear model are compared with direct numerical simulations of the original Navier-Stokes equations. The pipe flow code described in [67] has been used for simulation of full turbulence subject to a forcing f. This time stepping code also uses a Fourier decomposition in θ and x, but finite differences on a nonequispaced radial (y) nine-point stencil. Time steps are controlled using information from a second-order predictor-corrector method. For most simulations presented, the radial spacings are $\delta r_{\min}^+=0.11$, $\delta r_{\max}^+=4.4$ (wall units ν/u_τ). With dealiasing, $\delta_\theta^+=5.9$, $\delta_x^+=9.4$ at the boundary, in a domain $L=15(R)$, $L^+=2700$. Verification of these results is performed by calculation where the spacings above are respectively 0.08, 4.0, 3.9, 6.3 for $L=20$. Simulations enforce a fixed mass flux, consistent with previous analyses [54,68].

III. LINEAR AMPLIFICATION OF COHERENT STRUCTURES

A. Wave number dependence

We first consider the dependence of the optimal amplifications on the streamwise and azimuthal wave numbers at the very large flux-Reynolds number of $Re=10^6$ corresponding to $Re_\tau=19\,200$. Figure 1 shows the dependence of $G_{\max}$, $R_{\max}$ and V on m for the selected $\alpha=0,1,10,100,1000$. It is clear from all plots that streamwise elongated structures, where $\lambda_x>\lambda_\theta$, are significantly amplified. The greatest growths are found for axially independent modes ($\alpha=0$), for which the curve provides an envelope over the results for nonzero α. The maxima on the $\alpha=0$ curves are for $m=1$ azimuthal symmetry. The inset to Fig. 1(b) shows that steady forcing is optimal for axially independent harmonic forcing, $\alpha=0$, while for streamwise nonuniform perturbations, a nonzero forcing frequency is optimal. For the stochastic forcing at the optimal value $\alpha=0$, $m=1$, it is found that the leading Karhunen-Loève mode dominates, representing 93% of the contribution to the total variance, as reported in the inset to Fig. 1(c).

A secondary peak occurs in $G_{\max}$ at a larger m corresponding to an azimuthal wavelength of $\lambda_\theta^+=92$ (wall units ν/u_τ). Contrary to the optimal growth of initial conditions,
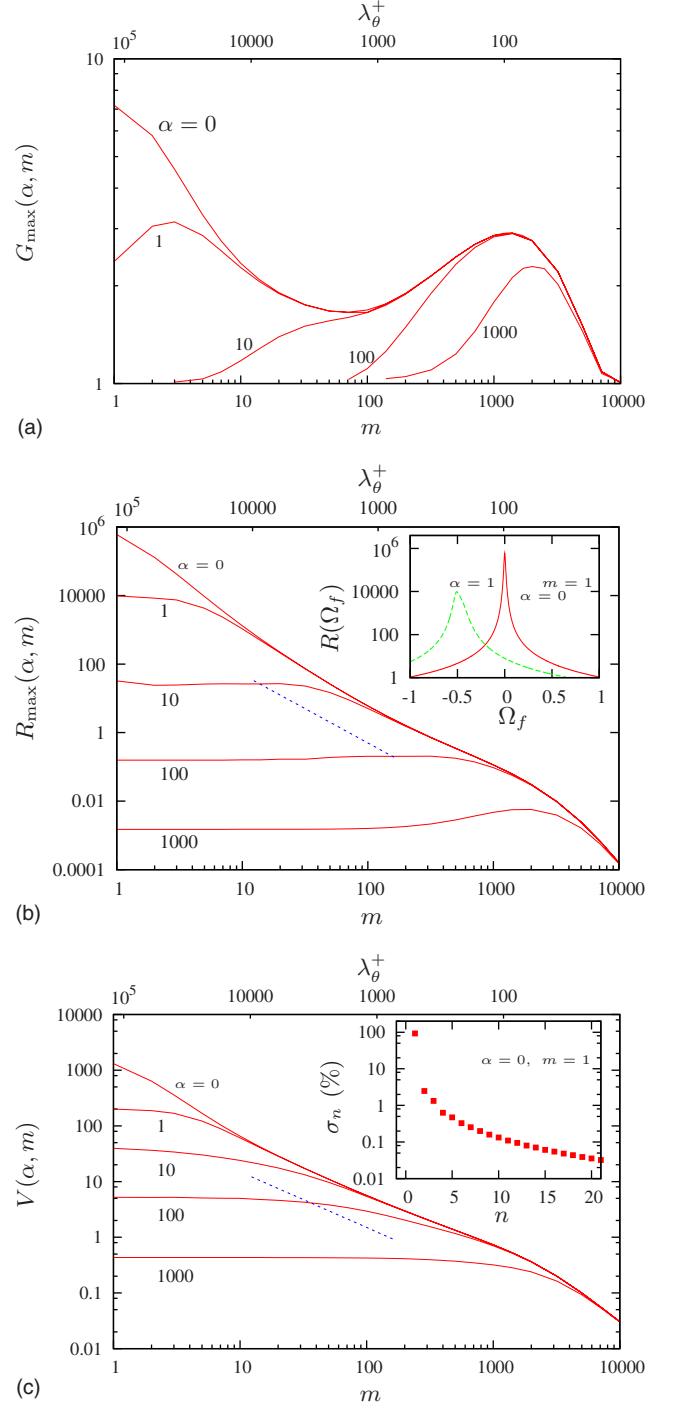

FIG. 1. (Color online) Optimal energy growth of initial conditions $G_{\max}$ (a), optimal response to harmonic forcing $R_{\max}$ (b) and variance of the response to stochastic forcing V (c) for $Re_\tau=19200$. Dependence on azimuthal wave number m, with corresponding wavelength in wall units λ_θ^+ (top axis), for selected values of the dimensionless streamwise wave number α. Reference slopes m^{-2} and m^{-1} (dotted lines) are shown in subfigures (b) and (c) respectively. The dependence of the optimal harmonic forcing amplification $R(\alpha,m=1;\Omega_f)$ on the forcing frequency Ω_f is reported in the insert of subfigure (b) for $\alpha=0$ and $\alpha=1$; $R_{\max}=\max_{\Omega_f} R$. The percentage contribution to the variance, $100\sigma_j/V(0,1)$, of the response to stochastic forcing contained in the first 20 Karhunen-Loève modes is reported in the insert of subfigure (c).
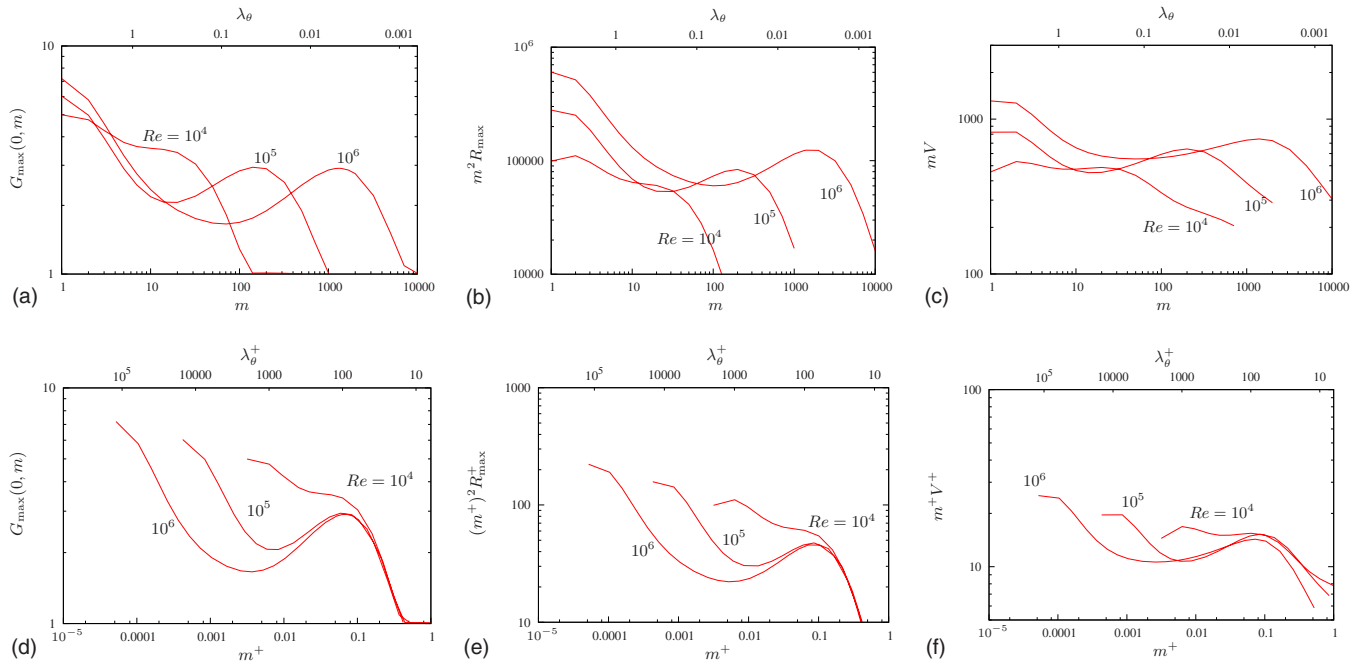
FIG. 2. (Color online) Dependence on the azimuthal wave number m and the corresponding azimuthal wavelength (top axis) of: the optimal energy amplification of initial condition G_{max} [(a) and (d)], the premultiplied optimal response to harmonic forcing $m^2 R_{max}$ [(b) and (e)] and of the premultiplied variance of the response stochastic forcing mV [(b) and (e)]. Streamwise uniform ($\alpha=0$) perturbations are considered for the selected Reynolds numbers Re=10^4, 10^5 and 10^6 corresponding to Re$_\tau$=317, 2830, and 19200. The responses, wave numbers and wavelengths are scaled in outer units on the upper row [(a), (b), and (c)] and in inner units in the lower row [(d), (e), and (f)].

no secondary peak is found in the optimal response to forcing. A closer examination of Figs. 1(b) and 1(c) reveals that the R_{max} and V curves corresponding to $\alpha=0$ scale approximatively like m^{-2} and m^{-1}, respectively, for intermediate values of m. A noticeable change of slope is found for values of m corresponding to $\lambda_\theta^+ \approx 100$. In plane channel flow, this power-law dependence has been explicitly related to the behavior of geometrically similar optimal structures in the log-layer [26]. In the case of the response to forcing, primary and secondary peaks occur in the deviations from this power-law behavior [26]. This can be seen by considering the premultiplied responses $m^2 R_{max}$ and mV. A secondary peak at λ_θ^+ =73 is found in the premultiplied response curves for $\alpha=0$, shown in Figs. 2(b) and 2(c).

B. Reynolds number dependence

The spanwise optimal wave numbers, corresponding to the primary and to the secondary peak, do not change with Re when, respectively, scaled with outer and inner units. This can be seen in Fig. 2, where G_{max} and the premultiplied

$m^2 R_{max}$, mV computed for Re=10^4, 10^5, and 10^6 (corresponding to Re$_\tau$=317, 2380, and 19 200, respectively) for $\alpha=0$ are reported. While the premultiplied response to steady forcing is useful for showing deviations from the R_{max} $\sim m^{-2}$ trend, the premultiplied stochastically forced case is arguably more representative of turbulence. When m is presented on a log scale, equal area under the curve mV implies equal contribution to the total variance. Here, where the spanwise wave number is integer for pipe flow, all the primary peaks are reached for $m=1$ except for the premultiplied stochastic response at lower Re$_\tau$; for Re$_\tau$=10^4, $m=2$ is preferred and the selection of m is very weak in mV for Re =10^4 and lower. The secondary peak is always found at λ_θ^+ ≈ 70–90 for all the premultiplied responses. The primary and the secondary peaks, however, are not yet separated at Re$_\tau$=10^4, while they are for Re$_\tau$=10^5 and higher, in good accordance with the turbulent plane channel [24–26] the boundary layer [27].

The maximum responses, associated with the primary peak ($\alpha=0$, $m=1$) increase with the Reynolds number, while those associated with the secondary peak remain almost constant. The structure of the leading modes corresponding to
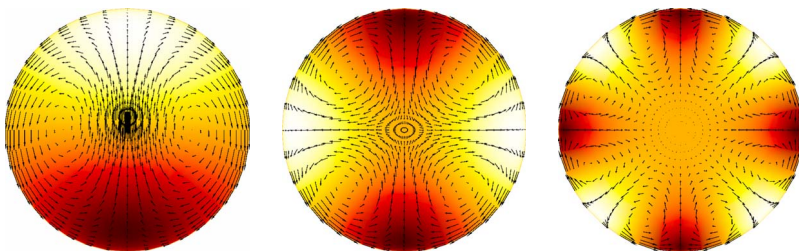

FIG. 3. (Color online) Linear optimal responses to steady forcing for $\alpha=0$ and m =$1, 2, 4$; Re$_\tau$=19200. Vectors: cross-stream components of the input vector field. (Colored) contour levels: streamwise component of the output field (streaks). White fast-streaks, red/dark slow streaks.
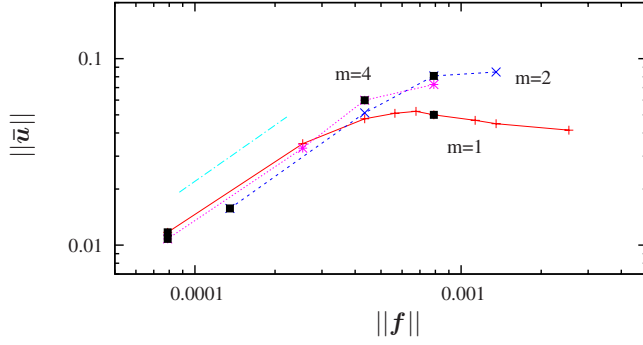
FIG. 4. (Color online) Response to forcing in full simulation showing the linear régime and nonlinear saturation. $\|f\|$ is the rms value. The isolated line is of slope 1 and squares correspond to the plots of Fig. 5.

the primary peak for optimal growth, for the response to steady and stochastic forcing, appear to be almost identical and remain the same over the entire range of Reynolds numbers. Plotted in Fig. 3 are the leading modes for $m=1,2,4$ (data from the optimal harmonic forcing case at Re$=10^6$). The optimal input consists of the expected large-scale streamwise vortices and the optimal output of large-scale streamwise streaks. Note that in this geometry, only modes of $m=1$ can exhibit flow across the axis. The structures corresponding to the secondary peak, which scale in inner units, are almost indistinguishable from those found in the plane channel and the boundary layer [25–27] and are therefore not reported here.

IV. SIMULATION OF FORCED FINITE AMPLITUDE COHERENT STREAKS

A. Response to finite amplitude optimal steady forcing

The optimal response predictions, described in the previous section, were based on two main simplifying assumptions: (a) the effect of the uncorrelated motions was modeled with an isotropic eddy-viscosity and (b) coherent perturbations were assumed small. We now test the level of approxi-

mation implied in these assumptions by computing in full DNS the effective responses of the predicted optimal perturbations. In particular, we consider the response to the optimal steady large-scale forcing, the mode which is the most amplified, and potentially the most relevant for passive flow control applications. The forcing term f is taken to be proportional to the mode $\widetilde{f}$ that optimizes $R_{\max}$, obtained from the above linear analysis, for $\alpha=0$ and a given m. As the considered optimal forcing is steady, time averages can be easily calculated and the statistical convergence readily checked. The magnitude of the steady forcing $\|f\|$ is measured by the rms value, as before. The response of the flow in simulations is given by $\bar{u}(r,\theta)=\langle u \rangle_{x,t}-\bar{U}(r)\hat{x}$, where $\bar{U}(r)=\langle u \rangle_{\theta,x,t}$ is the mean flow in the absence of forcing. $\langle \cdot \rangle_s$ indicates averaging over the subscripted variables. Averages are taken over at least $2800R/U_{cl}^{lam}$ time units. The DNSs are performed at Re$=5300$, for which Re$_\tau=180$.

From Fig. 4 it is seen that the amplitude of the responses $\|\bar{u}\|$ depends linearly on the forcing for small forcing amplitudes $\|f\|$. Small forcing can lead to large responses, in agreement with the linear eddy-viscosity model and, in the linear régime, the leading mode is $m=1$, as expected. The response predicted by the linear eddy-viscosity model is $R_{\max}=276^2$ for $m=1$ at this Re, while in the simulations, $\|\bar{u}\|/\|f\|$ is a factor 2 smaller than expected in the linear range. As the time-averaged mean flow for the unforced case, obtained from DNS, deviates very little from that given by Eqs. (2) and (1), this difference is most likely attributed to the isotropic eddy-viscosity assumption. Similar considerations apply to the observation that the $m=4$ mode is slightly more responsive than the $m=2$ mode in the linear regime.

For larger forcing amplitude, the amplitude of response saturates. For the $m=1$ mode, this saturation begins when the amplitude A_S of the associated coherent streaks is near to 19% of the center-line speed, where $A_S=\frac{1}{2}(\max \bar{u}_x - \min \bar{u}_x)$ [69]. The responses to higher order optimal modes ($m=2$ and $m=4$) saturate at larger forcing amplitudes $\|f\|$, and therefore contain more energy $\|\bar{u}\|^2$ than the $m=1$ mode, for sufficiently large forcing amplitudes.

In Fig. 5, we report the finite amplitude coherent vortices and streaks induced by the steady forcing for, respectively,
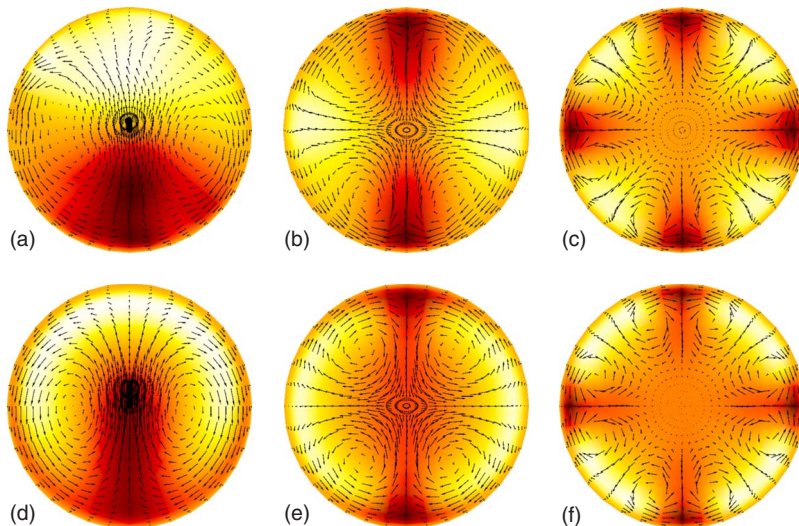

FIG. 5. (Color online) Nonlinear responses to finite amplitude forcing for $\alpha=0$ and $m=1,2,4$ from direct numerical simulation at Re$_\tau=180$. Small forcing amplitude (upper row) and moderate forcing (lower row), corresponding to the marked squares in Fig. 5. (a) $m=1$, $\|f\|=8.0 10^{-5}$; (b) $m=2$, $\|f\|=1.4 10^{-5}$; (c) $m=4$, $\|f\|=8.0 10^{-5}$; (d) $m=1$, $\|f\|=8.0 10^{-4}$; (e) $m=2$, $\|f\|=8.0 10^{-4}$; (f) $m=4$, $\|f\|=2.5 10^{-4}$. Vectors: cross-stream components of the forced velocity field. (Colored) contour levels: streamwise component of the output field (streaks). White fast-streaks, red/dark slow-streaks.
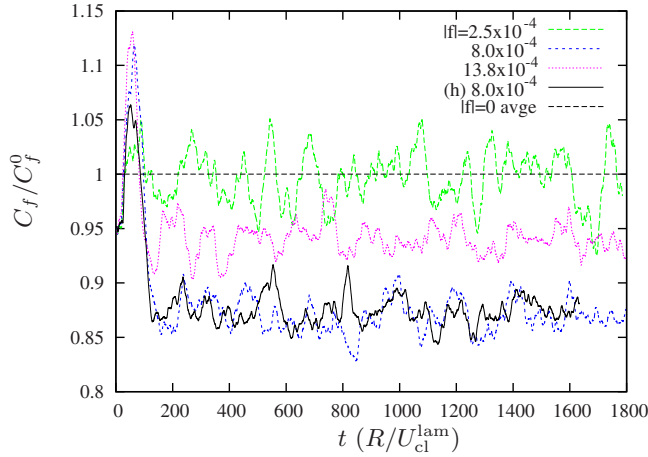
FIG. 6. (Color online) Relative drag for several levels of steady forcing of the $m=1$ mode from direct numerical simulation. At intermediate levels of forcing the drag is reduced, falling below the average of the unforced case (horizontal straight line). The forcing can reduce the drag. The solid line is a higher resolution check at $\|f\|=8.0 10^{-4}$.

low and moderate forcing amplitudes for the three azimuthal modes $m=1$, $m=2$, and $m=4$. From these figures, and by comparing them with the linear optimals reported in Fig. 3, it is seen how, for increasing forcing amplitude, the low-speed streaks are more and more spatially concentrated, while high-speed streaks have a tendency to widen.

B. Influence on the drag

We now examine the influence of the forced finite amplitude streaks on the drag, always at Re=5300 (corresponding to Re$_\tau$=180). Figure 6 shows time series for the instantaneous $C_f=2(u_\tau/U_b)^2$ in full DNS for three levels of optimal steady forcing of the $m=1$, $\alpha=0$ mode. In wall units, the spanwise wavelength of the forced streaks for $m=1$ is $\lambda_\theta^+ \approx 1130$, which extends by a factor greater than 2 the spacings considered in earlier investigations of the plane channel flow [54,55]. The horizontal line in Fig. 6 represents the baseline (time averaged) C_f in the absence of forcing. From this figure we see that indeed average drag reductions can be obtained also in the turbulent pipe flow. We have verified the accuracy of this result, in particular that no loss of the observed drag occurs (solid line), by performing an additional calculation at higher resolution (more than doubling the number of grid points, see Sec. II D).

In Fig. 7, the relative change for time averaged C_f is reported versus the forcing amplitude for the $m=1$, $m=2$, and $m=4$ modes. Drag reduction is obtainable over a range of forcing amplitudes covering approximately one order of magnitude. Selecting the best forcing amplitude, the maximum drag reduction achieved is 12.8% when forcing the $m=1$ mode. It is reduced for higher modes, e.g., 10.4% for $m=2$ ($\lambda_\theta^+ \approx 565$) and 4% for the mode $m=4$ ($\lambda_\theta^+ \approx 280$). Forcing streaks at the near-wall peak mean spacing ($\lambda_\theta^+=100$, corresponding to $m \approx 12$) results in increased drag.

For this control strategy to be interesting for applications, the net power saved must be considered. The power con-
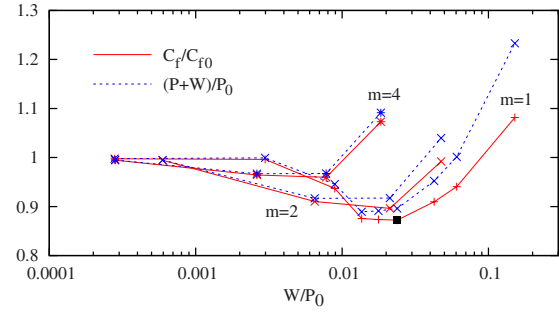

FIG. 7. (Color online) Effect of forcing on the mean skin friction, relative to the unforced case (solid). Relative net power consumption including the work done by the force (dashed). Black square corresponds to $\|f\|=8.0 10^{-4}$.

sumption (per unit length) spent to maintain the desired constant volume flux of the turbulent flow is $P=\frac{\pi}{8}C_f$ in units $\rho U_{cl}^{lam3} R$, and the control power spent (per unit length) to maintain the vortices is $W=\frac{1}{L}\int u \cdot f dV$. The drag relative to the unforced case is then given by $C_f/C_{f0}=P/P_0$, and the total relative net power consumption by $(P+W)/P_0$. The percentage net power saving is thus $100[1-(P+W)/P_0]$. From Fig. 7, where the relative drag and net power consumption are shown versus the forcing power, it is seen that the best net power saving corresponds to 11.1% and is obtained for the $m=1$ mode. For this case, W is only 1.4% of P_0. The response to forcing the large-scale mode is large, and as a result little energy is required to generate the prominent large-scale slow streak which affects the drag at the walls. The forcing of higher optimal modes results in smaller net power savings (e.g., at best 8.3% for $m=2$ and 3.3% for $m=4$).

The drag reducing mechanism appears to be consistent with that observed in plane channel flow [54,55]. Figure 8(a) shows a snapshot of streamwise vorticity field in the absence of forced streaks. Intense small-scale quasistreamwise vortices with $\lambda_\theta^+ \approx 100$ appear irregularly but in the whole azimuthal domain. These vortices, largely responsible for the turbulent skin friction [70], are weakened when large-scale streaks are artificially forced, and are almost suppressed from the high-speed streak region as seen in Figs. 8(b) and 8(c). In
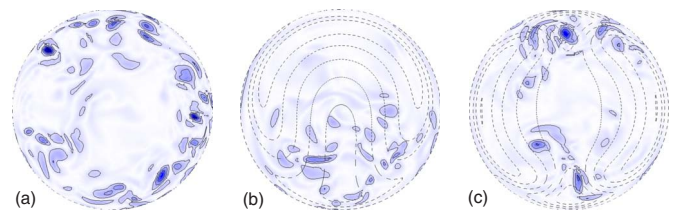

FIG. 8. (Color online) Snapshots of the cross-stream distribution of the streamwise vorticity ω_x field at a selected streamwise station from direct numerical simulation. (a) Streamwise vorticity in the absence of forcing. (b,c) Weakened and localized streamwise vorticity in the presence of the $m=1,2$ steady forcing, corresponding to optimal drag reduction. Blue/dark intense vorticity, white no vorticity. Same color scales are used on all the subplots. Contour lines denote isolevels of the streamwise averaged velocity (the forced streaks).

the absence of this mechanism the drag would only increase due to distortion of the mean flow by the forcing. This drag, however, only appears to be large for moderate to large amplitudes of the forcing, leading to the observed drag reduction for intermediate forcing.

V. SUMMARY AND CONCLUSIONS

The first part of this investigation was dedicated to the computation of the optimal linear energy amplifications of coherent structures supported by the turbulent pipe mean flow. The problem formulation and the tools used in the analysis follow those of investigations of the turbulent plane channel flow [24–26], Couette flow [28], and boundary layer flow [27]. In accordance with these investigations it is found that, despite the turbulent mean flow is linearly stable, it can support the energy amplification of initial conditions and of harmonic and stochastic forcing. These energy amplifications have the expected characteristics of the lift-up effect, where vortices amplify streaks and the most amplified perturbations are streamwise uniform ($\alpha=0$). For these streamwise uniform structures, at sufficiently large Re, the maximum energy amplifications are obtained for the $m=1$ azimuthal mode. Furthermore, this large amplification increases with the Reynolds number. As observed in the Couette and plane channel flow [26,28], for the three different calculations, the initial value problem, response to harmonic forcing and most energetic Karhunen-Loève mode for stochastic forcing, the optimal inputs and outputs almost coincide.

A secondary peak is found in the $G_{max}(m, \alpha=0)$ curves for the azimuthal mode corresponding to an azimuthal wave number $\lambda_\theta^+=92$, but only a change of slope in the $R_{max}(m, \alpha=0)$, $V(m, \alpha=0)$ curves is noticeable at this λ_θ^+. The responses R_{max} and V of optimal harmonic and stochastic forcing, for $\alpha=0$ decrease with the azimuthal wave number, with an approximate scaling of m^{-2} and m^{-1} respectively for intermediate m. For the plane channel flow, this inverse power dependence on the spanwise wave number has been related to the amplification of geometrically similar structures in the log-layer [26]. To highlight the departure of the optimal responses from the power-law trend, the premultiplied responses $m^2 R_{max}$ and mV have been considered. A secondary peak is then found at $\lambda_\theta^+=73$. This peak wavelength and the corresponding responses do not change with Reynolds number, provided that they are scaled in inner units, and that the Reynolds number is sufficiently large, so as to allow for a well defined inner-outer scale separation. The corresponding structures consist of streamwise uniform buffer-layer streaks and vortices.

The linear formulations we have used allowed a relatively straightforward computation of the linear optimal energy amplifications. The advantage of this model, based on the turbulent eddy viscosity, is therefore its simplicity, while quantitatively accurate predictions could be made with more sophisticated models. It is however important to verify that the predictions of the model, such as the order of magnitude of the growth of structures at large scale, or the fact that they more amplified than small-scale structures, are at least qualitatively verified. We have therefore reported the results of direct numerical simulations, where coherent structures have been artificially forced at the moderate $Re_\tau=180$. The optimal steady forcing of large-scale structures ($m=1$, $m=2$, and $m=4$) has been considered as these structures are the most responsive, and therefore are not only easier to detect, but are potentially most interesting for control purposes. The main predictions of the linear model are qualitatively observed in the DNS: the low-m optimal perturbations show a very large response in the amplitude of induced streaks. For sufficiently small forcing amplitudes, the response to forcing is linear and the azimuthal symmetries of the forced modes are well preserved in the response. In this linear regime, the $m=1$ mode is the most responsive. The agreement between the amplifications predicted by the linear model and the one observed in the DNS is only qualitative. The quantitative differences can probably be attributed to the very eddy-viscosity assumption and could probably be reduced by using a more realistic modeling of the Reynolds stresses. As coherent structures are strongly elongated in the streamwise direction, the isotropic eddy viscosity is gives only a first order approximation. At finite amplitudes of the coherent motions, the neglected interactions with the mean flow and the random turbulent field clearly become important [71]. For larger forcing amplitudes, a saturation in the amplitude of the forced response is observed. The $m=1$ mode is the first to saturate, at a considerable amplitude of almost 20% of the centerline velocity. For increasing amplitudes, the symmetry between the high and low-speed streaks is progressively lost. Low speed streaks concentrate in smaller spanwise extensions, with slightly larger amplitude, while high-speed streaks widen and slightly decrease in amplitude. This asymmetry recalls the observed "real" unforced turbulent flows [72].

The exact relation existing between optimally amplified streaks and the coherent structures populating the "natural" (unforced) turbulent pipe flow requires consideration. In the plane channel and Couette flows, the similarity of the spanwise scales selected by the linear mechanism and those observed in the actual turbulent flow is probably explained by the requirement that significant amplification is necessary for energetic turbulent processes to be self-sustained. What is currently not clear, because of the lack of experimental or numerical data, is if $m=1$ is the dominating coherent mode at sufficiently large Re. Most of the investigations of large- and very-large scale coherent motions in the pipe flow [19,20,73,74], have rather focused on the streamwise scales of these motions. If these motions arise through a self-sustaining process, then the streamwise scales of the motion would be selected by processes related to the breakdown of the streaks. This process is missing in the present analysis. What can be said with the model, however, is which azimuthal modes are most amplified for a streamwise scale selected by other stochastic processes. For instance, if one considers streamwise wavelengths ranging from $\lambda_x=16(R)$ ($\alpha \approx 0.4$) to $\lambda_x=6$ ($\alpha \approx 1$), then the most amplified structures vary from $m=2$ to $m=5$ modes at sufficiently large Re in the stochastic response. However, at even moderately low Reynolds number (e.g., $Re=10^4$ corresponding to $Re_\tau=317$), the azimuthal selection is weak and modes ranging from $m=1$ to $m=10$ all exhibit a comparable variance [see Fig. 2(c)] in the

integrated response. These predictions are compatible with recent results from direct numerical simulations at Re_τ =150 [75] where the most energetic POD modes are found for the streamwise wavelength $\lambda_x = 20(R)$ (the computational box size) and for azimuthal modes ranging from $m=2$ to $m=7$. Additional simulations or experiments would be highly desirable to examine the azimuthal structure of the most energetic modes at larger Re.

One of the most relevant applications of the optimal perturbations of the turbulent mean flows probably resides in flow control. The direct numerical simulations confirm that energy can be greatly amplified in a turbulent flow. An objective of both theoretical and practical relevance is the reduction of the power required to drive the constant mass flux through the pipe. Using optimal forcing, less than 2% of the power required to pump the (unforced) flow, is required to induce modifications in the mean flow of the order of 20% of the centerline mean velocity. Previous numerical [54] and experimental [55] studies have shown that it is possible to reduce the mean turbulent drag in the plane channel flow by forcing large-scale vortices with spanwise wavelength of ≈400–500 wall units. Here we have extended this result to pipe flow, where $\lambda_\theta^+ \approx 1200$ wall units for $m=1$. Mean drag reductions of ≈13% are achieved by forcing this $m=1$ mode, while the drag reduction is reduced for reduced spanwise spacing. In [54] the observed drag reduction was attributed to the mean weakening of the circulation of quasistreamwise coherent vortices. This effect on the quasistreamwise vortices is found in the present turbulent pipe flow. Our visualizations show that the quasistreamwise vortices of the "natural" buffer layer cycle are packed in the low-speed streak region, while they are essentially removed from the high-speed streak region.

At present it is not clear why the drag reduction reduces as the spanwise spacing is reduced. It is possible that for $m=2$ ($\lambda_\theta^+ \approx 600$) the reduced scale separation from that of the naturally occurring streaks ($\lambda_\theta^+ \approx 100$) causes the drag-reduction effect to be reduced. At spanwise separations greater than those possible at this Re_τ, where clear scale separation occurs, a plateau in the drag reduction is possible for separations greater than $\lambda_\theta^+ \approx 1200$. However, if the greatest reduction continues to be observed for the largest possible spacing, here $m=1$, it may be conjectured that, rather than scaling in inner units, the mode that most reduces drag has an upper limit that depends on the geometry. Additional simulations or new experiments at much larger Re_τ could confirm or reject these conjectures.

We have also extended earlier investigations by computing the net power saving obtained by forcing the optimal coherent streaks. As these streaks are optimal, the power required to force them is already almost minimized. Even at the considered low Reynolds number, the controlling streaks are forced with less than 2% of the power necessary to maintain the base flow, and a net power saving of ≈11% is achieved with the $m=1$ mode. For useful implementation of the method proposed in this study, the induction of rolls need not be efficient. For example, efficiency of 50%, still using only 4% of the driving energy, might be acceptable. Note also that, as the amplification of the forcing is expected to increase with increasing Re, the percentage of total power

used to force the streaks is predicted to *decrease* for increasing Re. In practice, induction of large-scale rolls is possible via passive actuators in laminar [49,50,76] and turbulent flows [51–53]. Although neither would reproduce the precise details of forcing used here, linear optimals are known to be robust to perturbations of the system, and responses close to those seen here can be expected. An experimental verification of the proposed control strategy would of course be very welcome.

APPENDIX A: RADIALLY-DEPENDENT VISCOSITY

For the radially dependent effective viscosity, $\nu_T(r)$, the viscous terms in Eq. (3) are given by

$$\nabla \cdot [\nu_T(r)(\nabla \boldsymbol{u} + \nabla \boldsymbol{u}^T)] = \nu_T \nabla^2 \boldsymbol{u}$$

$$+ \partial_r \nu_T \cdot \begin{bmatrix} 2\partial_r u_r \\ \partial_r u_\theta - \dfrac{1}{r}u_\theta + \dfrac{1}{r}\partial_\theta u_r \\ \partial_x u_r + \partial_r u_x \end{bmatrix},$$

(A1)

where

$$\nabla^2 \boldsymbol{u} = \begin{bmatrix} \nabla^2 u_r - \dfrac{2}{r^2}\partial_\theta u_\theta - \dfrac{u_r}{r^2} \\ \nabla^2 u_\theta + \dfrac{2}{r^2}\partial_\theta u_r - \dfrac{u_\theta}{r^2} \\ \nabla^2 u_x \end{bmatrix}.$$

(A2)

APPENDIX B: NUMERICAL CONSIDERATIONS

Cumbersome differential operations in cylindrical coordinates, particularly given $\nu_T = \nu_T(r)$, mean that finding the Orr-Somerfield form for Eq. (B2) is not straight forward in this geometry. Instead, for this study the continuity equation together with Eq. (3) have been used directly in primitive variable form, giving the generalized eigenvalue problem

$$\mathbf{X}\hat{\phi} = -\sigma \mathbf{Y}\hat{\phi}, \tag{B1}$$

where $\phi(r;t) = \hat{\phi}(r)e^{\sigma t}$. Note that **Y** is singular, containing three zero boundary conditions and a zero right hand side for the continuity condition. Simplifications can be made by observing that **X** is invertible, and that, as the σ have real part strictly less than zero, Eq. (B1) can be written in the standard form, $(-1/\sigma)\hat{\psi} = (\mathbf{X}^{-1}\mathbf{Y})\hat{\psi}$. Standard LAPACK routines return the leading eigenvalues along with a predicable number of infinite eigenvalues that are easily filtered. Excellent numerical stability is observed.

The continuity equation together with the linearized Eq. (3) and no-slip boundary conditions can be written in the form

$$u = \mathbf{V}x,$$

$$\partial_t x = \Lambda x + \mathbf{W}f, \tag{B2}$$

where x is an alternative representation for the state space ϕ. Conversion between the representations is performed by the action of $\mathbf{V}$ and $\mathbf{W}$. This form is again familiar through the Orr-Somerfield formulation of the governing equations. Here, however, the eigenfunction decomposition is employed. Matrix $\mathbf{V}$ has columns of eigenvectors $\hat{u}_n$ and $\Lambda = \text{diag}(\sigma_n)$, with the σ_n arranged in descending order. These matrices, along with the diagonal weight matrix $\mathbf{M}$ s.t. $\|u\|^2 \equiv u^H \mathbf{M}u$, are sufficient to calculate optimally growing initial conditions.

Consider the norm for x given by $\|u\|^2 = x^H \hat{\mathbf{M}} x \equiv \|x\|^2 = (x, x)$, where $\hat{\mathbf{M}} = \mathbf{V}^H \mathbf{M}\mathbf{V}$. The optimal initial condition x_0

for growth at time t satisfies $G(t) = (\mathbf{A}x_0, \mathbf{A}x_0)/(x_0, x_0) = (\mathbf{A}^+\mathbf{A}x_0, x_0)/(x_0, x_0)$, where the transfer function for x is $\mathbf{A} = e^{t\Lambda}$ and the adjoint can be shown in a few operations to be $\mathbf{A}^+ = \hat{\mathbf{M}}^{-1}\mathbf{A}^H\hat{\mathbf{M}}$. The growth and initial condition can be calculated by power iteration on the matrix $\mathbf{A}^+\mathbf{A}$. This matrix is straight-forward to evaluate when Λ is diagonal.

Calculation of the optimal harmonic forcing requires only minor alterations to the above. In this case one uses $\mathbf{A} = (i\Omega_f \mathbf{I} - \Lambda)^{-1}$, which is again a diagonal matrix for Λ diagonal.

For the stochastic response, it can be shown [65] that $\mathbf{C}_\infty = \mathbf{V}\mathbf{G}_\infty \mathbf{V}^H$, where $\mathbf{G}_\infty$ solves the Lyapunov equation

$$\Lambda \mathbf{G}_\infty + \mathbf{G}_\infty \Lambda^H + \mathbf{W}\mathbf{W}^H = \mathbf{0}. \tag{B3}$$

For $\mathbf{W}$ one may take the Moore-Penrose pseudoinverse of $\mathbf{V}$. (Singularity of $\mathbf{Y}$ leads to fewer columns of eigenvectors than rows in $\mathbf{V}$.) MATLAB routines are then available to solve Eq. (B3).

---

[1] O. Reynolds, Proc. R. Soc. London **35**, 84 (1883).

[2] H. K. Moffatt, in *Proceedings of the URSI-IUGG Colloquium on Atomspheric Turbulence and Radio Wave Propagation*, edited by A. Yaglom and V. I. Tatarsky (Nauka, Moscow, 1967), pp. 139–154.

[3] M. T. Landahl, J. Fluid Mech. **98**, 243 (1980).

[4] S. C. Reddy and D. S. Henningson, J. Fluid Mech. **252**, 209 (1993).

[5] L. N. Trefethen, A. E. Trefethen, S. C. Reddy, and T. A. Driscoll, Science **261**, 578 (1993).

[6] P. J. Schmid and D. S. Henningson, *Stability and Transition in Shear Flows* (Springer, New York, 2001).

[7] L. H. Gustavsson, J. Fluid Mech. **224**, 241 (1991).

[8] K. M. Butler and B. F. Farrell, Phys. Fluids A **4**, 1637 (1992).

[9] B. F. Farrell and P. J. Ioannou, Phys. Fluids A **5**, 2600 (1993).

[10] L. Bergström, Stud. Appl. Math. **87**, 61 (1992).

[11] L. Bergström, Phys. Fluids A **5**, 2710 (1993).

[12] P. Schmid and D. S. Henningson, J. Fluid Mech. **277**, 197 (1994).

[13] O. Y. Zikanov, Phys. Fluids **8**, 2923 (1996).

[14] S. J. Kline, W. C. Reynolds, F. A. Schraub, and P. W. Runstadler, J. Fluid Mech. **30**, 741 (1967).

[15] J. R. Smith and S. P. Metzler, J. Fluid Mech. **129**, 27 (1983).

[16] J. C. Klewicki, M. M. Metzger, E. Kelner, and E. M. Thurlow, Phys. Fluids **7**, 857 (1995).

[17] M. K. Lee, L. D. Eckelman, and T. J. Hanratty (1974).

[18] B. U. Achia and D. W. Thompson, J. Fluid Mech. **81**, 439 (1977).

[19] K. C. Kim and R. Adrian, Phys. Fluids **11**, 417 (1999).

[20] M. Guala, S. E. Hommema, and R. J. Adrian, J. Fluid Mech. **554**, 521 (2006).

[21] K. M. Butler and B. F. Farrell, Phys. Fluids A **5**, 774 (1993).

[22] B. F. Farrell and P. J. Ioannou, Phys. Fluids **5**, 1390 (1993).

[23] B. F. Farrell and P. J. Ioannou, Theor. Comput. Fluid Dyn. **11**, 237 (1998).

[24] J. C. del Álamo and J. Jiménez, J. Fluid Mech. **559**, 205 (2006).

[25] G. Pujals, M. García-Villalba, C. Cossu, and S. Depardon, Phys. Fluids **21**, 015109 (2009).

[26] Y. Hwang and C. Cossu, J. Fluid Mech. (to be published).

[27] C. Cossu, G. Pujals, and S. Depardon, J. Fluid Mech. **619**, 79 (2009).

[28] Y. Hwang and C. Cossu, J. Fluid Mech. **643**, 333 (2010).

[29] W. C. Reynolds and A. K. M. F. Hussain, J. Fluid Mech. **54**, 263 (1972).

[30] F. Waleffe, Phys. Fluids **7**, 3060 (1995).

[31] W. Schoppa and F. Hussain, J. Fluid Mech. **453**, 57 (2002).

[32] J. Hamilton, J. Kim, and F. Waleffe, J. Fluid Mech. **287**, 317 (1995).

[33] F. Waleffe, Stud. Appl. Math. **95**, 319 (1995).

[34] M. Nagata, J. Fluid Mech. **217**, 519 (1990).

[35] F. Waleffe, Phys. Rev. Lett. **81**, 4140 (1998).

[36] G. Kawahara and S. Kida, J. Fluid Mech. **449**, 291 (2001).

[37] H. Faisst and B. Eckhardt, Phys. Rev. Lett. **91**, 224502 (2003).

[38] H. Wedin and R. Kerswell, J. Fluid Mech. **508**, 333 (2004).

[39] N. V. Nikitin, Fluid Dyn. **44**, 652 (2009).

[40] F. Waleffe, J. Fluid Mech. **435**, 93 (2001).

[41] B. Eckhardt, T. Schneider, B. Hof, and J. Westerweel, Annu. Rev. Fluid Mech. **39**, 447 (2007).

[42] B. Hof, C. van Doorne, J. Westerweel, F. Nieuwstadt, H. Faisst, B. Eckhardt, H. Wedin, R. Kerswell, and F. Waleffe, Science **305**, 1594 (2004).

[43] J. F. Gibson, J. Halcrow, and P. Cvitanovic, J. Fluid Mech. **611**, 107 (2008).

[44] T. M. Schneider, J. F. Gibson, and J. Burke, Phys. Rev. Lett. **104**, 104501 (2003).

[45] D. Viswanath, Philos. Trans. R. Soc. London, Ser. A **367**, 561 (2009).

[46] C. C. T. Pringle, Y. Duguet, and R. R. Kerswell, Philos. Trans. R. Soc. London, Ser. A **367**, 457 (2009).

[47] C. Cossu and L. Brandt, Phys. Fluids **14**, L57 (2002).

[48] C. Cossu and L. Brandt, Eur. J. Mech. B/Fluids **23**, 815 (2004).

[49] J. Fransson, L. Brandt, A. Talamelli, and C. Cossu, Phys. Fluids **17**, 054110 (2005).

[50] J. H. M. Fransson, A. Talamelli, L. Brandt, and C. Cossu, Phys. Rev. Lett. **96**, 064501 (2006).

[51] G. Pujals, C. Cossu, and S. Depardon, *Sixth Symposium on Turbulence and Shear Flow Phenomena* (Seoul National University, Seoul, Korea, 2009).

[52] G. Pujals, C. Cossu, and S. Depardon, J. Turbul. (to be published).

[53] G. Pujals, S. Depardon, and C. Cossu, Exp. Fluids (to be published).

[54] S. Schoppa and F. Hussain, Phys. Fluids **10**, 1049 (1998).

[55] G. Iuso, M. Onorato, P. G. Spazzini, and G. M. di Cicca, J. Fluid Mech. **473**, 23 (2002).

[56] S. A. Orszag and A. T. Patera, J. Fluid Mech. **128**, 347 (1983).

[57] M. Quadrio and S. Sibilla, J. Fluid Mech. **424**, 217 (2000).

[58] R. D. Cess, Westinghouse Research Report No. 8–0529–R24, 1958 (unpublished).

[59] W. C. Reynolds and W. G. Tiederman, J. Fluid Mech. **27**, 253 (1967).

[60] B. J. McKeon, M. V. Zagarola, and A. J. Smits, J. Fluid Mech. **538**, 429 (2005).

[61] B. F. Farrell and P. J. Ioannou, J. Atmos. Sci. **53**, 2025 (1996).

[62] B. Bamieh and M. Dahleh, Phys. Fluids **13**, 3258 (2001).

[63] M. R. Jovanović and B. Bamieh, J. Fluid Mech. **534**, 145 (2005).

[64] P. Schmid, Annu. Rev. Fluid Mech. **39**, 129 (2007).

[65] K. Zhou, J. Doyle, and K. Glover, *Robust and Optimal Control* (Prentice Hall, New York, 1996).

[66] E. Lauga and C. Cossu, Phys. Fluids **17**, 088106 (2005).

[67] A. P. Willis and R. R. Kerswell, Phys. Rev. Lett. **100**, 124501 (2008).

[68] A. P. Willis and R. R. Kerswell, J. Fluid Mech. **619**, 213 (2009).

[69] P. Andersson, L. Brandt, A. Bottaro, and D. Henningson, J. Fluid Mech. **428**, 29 (2001).

[70] A. G. Kravchenko, H. Choi, and P. Moin, Phys. Fluids A **5**, 3307 (1993).

[71] Y. Lifshitz, D. Degani, and A. Tumin, Flow, Turbul. Combust. **80**, 61 (2008).

[72] C. D. Tomkins and R. J. Adrian, J. Fluid Mech. **490**, 37 (2003).

[73] W. R. B. Morrison and R. E. Kronauer, J. Fluid Mech. **39**, 117 (1969).

[74] K. J. Bullock, R. E. Cooper, and F. H. Abernathy, J. Fluid Mech. **88**, 585 (1978).

[75] A. Duggleby, K. S. Ball, and M. Schwaenen, Philos. Trans. R. Soc. London, Ser. A **367**, 473 (2009).

[76] J. Fransson, L. Brandt, A. Talamelli, and C. Cossu, Phys. Fluids **16**, 3627 (2004).